

# TUMBLING CHARACTERIZATION OF RESIDENT SPACE OBJECTS FROM GROUND-BASED OBSERVATIONS

M.A. De Luca<sup>(1)</sup>, R. Cipollone<sup>(1)</sup>, M.F. Montaruli<sup>(1)</sup>, M. Massari<sup>(1)</sup>, P. Di Lizia<sup>(1)</sup>, F. Bunkheila<sup>(2)</sup>, L. Spazzacampagna<sup>(2)</sup>, and A. Di Cecco<sup>(3)</sup>

<sup>(1)</sup>Department of Aerospace Science and Technology, Politecnico di Milano, Via G. La Masa 34 (20156), Milan, Italy, Email: {mariaalessandra.deluca, riccardo.cipollone, marcofelice.montaruli, mauro.massari, pierluigi.dilizia}@polimi.it

<sup>(2)</sup>Telespazio Spa, Via Tiburtina 965 (00156), Rome, Italy, Email: {federico.bunkheila, luca.spazzacampagna}@telespazio.com

<sup>(3)</sup>Agenzia Spaziale Italiana (ASI), Via del Politecnico snc (00133), Rome, Italy, Email: alessandra.dicecco@asi.it

## ABSTRACT

In recent years, the growing number of Resident Space Objects (RSOs) has raised major concerns due to the increasing risks of potential collisions in space and uncontrolled re-entries on Earth. Tackling this issue requires an effective characterization of orbiting objects, in terms of orbital and rotational motion, using sensor observations. However, accurately determining an object attitude remains a significant challenge due to factors such as measurement noise, short observation windows, complex target shape, and material properties.

This work presents the RSO Characterization Module developed for the Italian Space Agency ASI-IHS infrastructure for space surveillance and tracking, under the Next Generation UE/PNRR framework. The module integrates existing and newly developed algorithms for tumbling characterization of RSOs, both known and unknown, using ground-based optical and radar sensor measurements. To verify its performance, extensive tests were executed on both simulated and real data.

Keywords: Space Situational Awareness; RSO Characterization; tumbling; ground-based sensors; frequency analysis.

## 1. INTRODUCTION

The growing volume of Resident Space Objects (RSOs), including active satellites, defunct spacecraft, and orbital debris, has raised serious global concerns in recent years. This increase in space traffic raises the likelihood of potential collisions in orbit and uncontrolled re-entries on Earth, posing risks to infrastructure, environment, and human safety. The situation is particularly alarming in densely populated orbital regions, such as the Low Earth Orbit (LEO) and Geostationary Orbit (GEO), where collisions could trigger a cascade effect, known as the Kessler Syndrome, rendering these orbits unusable

for future missions. Thus, without effective mitigation strategies, space could become inaccessible within a few decades.

Addressing this issue requires effective characterization of orbiting objects, both in terms of orbit determination and reconstruction of rotational motion from sensor data. This is essential to enhance tracking accuracy, improve collisions and re-entries risk assessment, and inform on-orbit servicing and active debris removal strategies. However, unlike orbit determination, for which effective and well-established algorithms are already available [22], accurate attitude determination, especially for non-cooperative, uncatalogued objects, remains a significant challenge. Ground-based sensors, including optical systems, radar, and laser-ranging technologies, are key tools for this task. In particular, light curves, representing variations in apparent brightness over time, and Radar Cross Section (RCS) measurements, which capture signal reflections from the object, are both intrinsically linked to the rotational motion of the target [1]. However, besides factors such as measurement noise, short observation windows, and data gaps, this kind of measurements are further affected by the target shape and material properties. Consequently, most existing attitude determination studies focus on simple RSO shapes or rely on strong simplifying assumptions. Although these assumptions facilitate modeling and computation, they limit the applicability of the methods to case-specific scenarios.

This work aims to overcome the challenges just outlined for the characterization of tumbling RSOs, both known and unknown. Specifically, the RSO Characterization Module, developed for the Italian Space Agency ASI-IHS infrastructure for space surveillance and tracking under the Next Generation UE/PNRR framework, is presented. The module is designed to characterize a RSO tumbling state using either light curves or RCS measurements from ground-based optical and radar sensors. Unlike methods that focus on estimating the full attitude vector but are built on case-specific scenarios, the presented approach aims to extract key rotational features in a versatile way across different target types

and without requiring prior information, also exploiting well-established algorithms.

Specifically, the module primary outputs are estimates of the two apparent dominant periods of the input signal. One provides information on the rotation of the body about an extremal principal axis, while the other reflects the precession of this axis about the angular momentum vector. The pipeline can operate either with or without an initial guess for these quantities, accommodating cases with any prior knowledge of the target. However, it is important to note that any detected periods correspond to synodic periods rather than the satellite sidereal rotation periods.

The paper is organized as follows. Section 2 presents a review of the literature on RSOs tumbling motion characterization from ground-based measurements. Section 3 provides an overview of the developed pipeline. In Section 4, the performance of the pipeline is tested on both simulated and real measurements. Finally, Section 5 discusses the operational potential, identified limitations and planned future developments.

## 2. LITERATURE REVIEW ON RSO CHARACTERIZATION

Although several algorithms have been proposed in the literature, an accurate estimation of the full attitude vector remains challenging, especially without prior knowledge of the observed target. As a result, most algorithms are limited to estimating specific attitude-related quantities.

Among these, many documented techniques focus on estimating the rotation period of observed objects from the acquired signals, such as light curves or RCS time histories. Among the frequency domain techniques, the well-known Fast Fourier Transform (FFT) [3] decompose the signal into its constituent frequencies, allowing dominant periodicities to be identified. For unevenly spaced data, the Lomb-Scargle Periodogram [5] [6] offers a robust alternative. Another technique, still suitable for unevenly spaced data but operating in the time domain, is the Epoch Folding [7]. This algorithm divides the overall observation time into segments based on a guessed period, summing them to identify repeating patterns. A variant, the Phase Dispersion Minimization (PDM) [4], improves accuracy by dividing the data into bins and assessing the variance within each bin compared to the overall data variance. However, the major drawback of time domain techniques is their dependence on an initial guess of the period of the signal.

Delving into light curve analysis, several algorithms have been proposed to estimate not only the rotation period but also the orientation of the target spin axis. One such approach is the Amplitude Method [8], which is based on the ratio of the maximal and minimal brightness extracted from the light curve. Using another model based on the brightness ratio, [3] developed an algorithm

that estimates, in addition to the spin axis direction and rotation period, also its precession motion.

Another well-known approach is the Epoch Method [9]. The algorithm exploits the relation between the phase angle bisector (i.e. the vector that bisects the Sun-object-observer angle) time variation, expressed as a function of the spin axis orientation, and the satellite's sidereal and synodic periods. A more comprehensive technique, known as Light Curve Inversion [10], aims to estimate the full attitude state of an observed RSO. This method involves generating simulated light curves based on detailed object models and comparing them with observed data; an optimization algorithm minimizes the difference between the two to estimate the attitude state. However, this method typically requires initial conditions to guide the optimization process.

Finally, Machine Learning-based approaches have emerged as a promising tool in light curve analysis. For instance, in [11] a method to estimate the spin properties of satellites from their light curves is proposed, using a physics-based loss function in the learning objective.

Despite the variety of techniques available, all methods rely on certain assumptions. For example, the Amplitude Method assumes that the object has a cylindrical shape and is in a flat-spin motion [3] [8]. Only diffuse reflection is typically considered, and observation parameters such as target orbit and observation geometry are generally well known. Finally, for light curve inversion methods, additional knowledge about the target's geometry and material properties is typically required.

Alternatively to light curves, RCS measurements offer robustness against many optical limitations such as illumination and atmospheric conditions. RCS-based methods are relatively underexplored in the literature, but many of the algorithms discussed so far find application even in the radar case. Reference [12] developed a method that synthesizes RCS time series, which are then cross-correlated with RCS measurements obtained simultaneously from monostatic and bistatic radar systems, in order to estimate the object's attitude. Similarly, [13] proposes a method that matches simulated and real RCS time series (from different radar stations) using a hybrid particle swarm optimization algorithm.

As for light curve inversion algorithms, these techniques heavily depend on the availability of a detailed 3D model of the target, including its shape, material properties, and surface characteristics. Moreover, RCS signals are sensitive to the target's orientation relative to the radar and can exhibit significant variability even with small orientation changes.

Regardless of the sensor type used, all the methods presented so far require prior knowledge of the object rotational status (e.g., spinning or three-axis stabilized). When this information is unavailable, classification algorithms become essential. For instance, in [14], LEO objects are classified based on their stability using RCS statistics from Leolabs' global radar network. In [4], instead, a classification method based on light curve data is proposed. This approach utilizes the Lomb-Scargle Periodogram algorithm to extract the frequency spectrum

from the measurements. Classification is then performed by analyzing spectral features, and employing PDM technique to test candidate rotation periods.

Building on all these methods, this work presents a versatile pipeline for RSO tumbling characterization that can be applied regardless of whether information about the target object is available.

### 3. RSO CHARACTERIZATION MODULE: OVERVIEW

The RSO Characterization Module offers a method to estimate the characteristic periods of an object in orbit using measurements obtained from the ground, assuming that the object is in a rotational state. These measurements can be either brightness variations of the RSO over time (i.e., light curves), acquired by optical sensors, or its RCS variations over time, acquired by radar sensors. The following inputs are required by the processing pipeline:

- **Input signal:** the measured time-series data (light curve or RCS) and the corresponding time vector.
- **Filters flags:** Flags enabling or disabling optional pre-processing filters on the data, depending on data quality and operator requirements.
- **firstGuessflag:** When this flag is active, the user can optionally provide initial guesses for the tumbling periods. This capability is especially useful when prior knowledge of the RSO’s motion is available, as it can guide and potentially improve the convergence of the estimation algorithm.
- **SecondPeriodflag:** A control flag that selects one of the two modes described below.

The pipeline has two operative modes, and the number of outputs depends on the mode selected.

In the Mode #1, as illustrated in Fig. 1, the inputs are processed through the “First Period Estimation” block. Here, as further detailed in Section 3.1, a preliminary quality check is performed on the input data. If the checks are passed, the signal is pre-processed based on any activated filtering options. Next, the algorithm operates in the frequency domain by computing the Power Spectral Density (PSD) of the input signal. The local maxima (peaks) in the signal PSD are subsequently stored and post-processed. Finally, the peak most likely to be associated to the tumbling period of the object is identified, and the resulting value is returned to the user. If multiples of the period are also detected (due, for example, to a geometric symmetry in the target), they are also included in the output along with a warning message alerting the operator.

In the Mode #2, shown in Fig. 2, the pipeline adds a

time-domain optimization step to the frequency-domain analysis described above. Specifically, in the “Second Period Estimation” block, a two-dimensional Fourier series is fitted to the input data to identify a second significant period that is superimposed to the primary rotation, with the aim of obtaining a comprehensive assessment of the RSO rotational and precessional motion components. Along with the outputs from the first mode, this second mode returns the estimated secondary period and the Root Mean Square Error (RMSE) of the two-dimensional fit, allowing the user to assess the quality of the final solution.

In both modes, the pipeline provides as output a figure illustrating the processing performed. In particular, it shows the input signal, the pre-processed signal (if filters are applied), and the optimized signal (if the time-domain fit is executed).

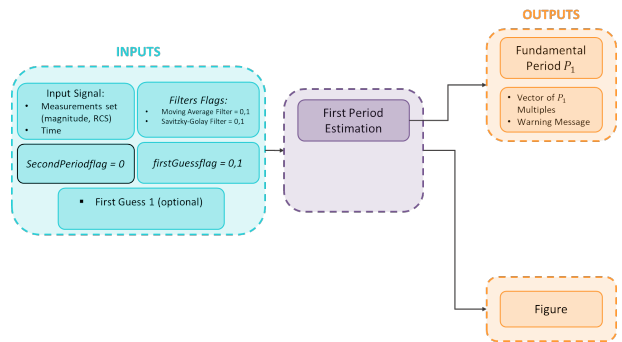


Figure 1. Overview of the RSO Characterization Module (Mode #1)

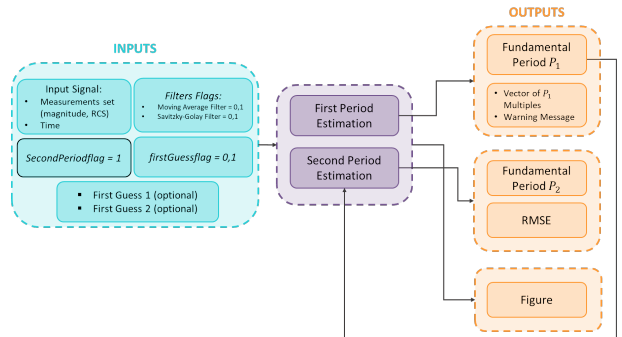


Figure 2. Overview of the RSO Characterization Module (Mode #2)

The two modes are better detailed in the following sections (Section 3.1 and Section 3.2 for Mode #1 and Mode #2, respectively).

#### 3.1. Mode #1

The module provides two possible pipelines: one applicable when an initial estimate of the period is available (Mode #1.1), and another for scenarios where no other information is available besides the measurements (Mode #1.2), as detailed below.

### Mode #1.1 : First Guess for $P_1$ Available

Fig. 3 refers to the scenario where an initial estimate of the tumbling period is available. To activate this pipeline, which starts at user's request, all that is required is to activate the *firstGuessflag*.

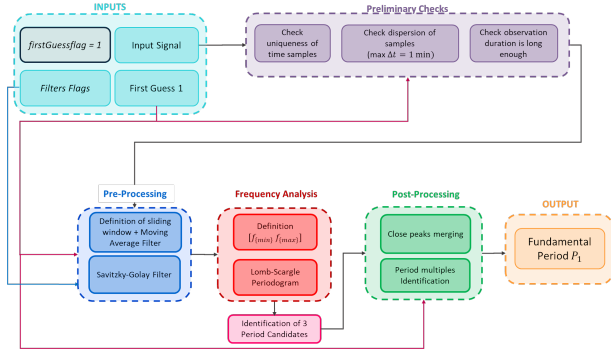


Figure 3. Flow Diagram (Mode #1.1)

As a first step, the “Preliminary Checks” block performs the following validations on the input signal:

- Ensure that all time samples are unique.
- Check that the samples are approximately evenly spaced. If the measurements present a time gap greater than one minute, the input signal is split into two (or more) portions and the portion with the longest duration is retained.
- Verify that the signal duration is sufficient. Specifically, the duration must be at least twice the provided initial estimate of the period.

If these checks are successfully passed, the signal is pre-processed. As previously mentioned, the user can control the pre-processing by enabling or disabling two separate flags: one for a moving average filter and the other for a Savitzky-Golay filter [16]. The former is used to detect and remove changes in the mean value of the signal, while the latter is used to filter out high-frequency noise. The initial estimate of the tumbling period is used to define the sliding window size in the moving average filter. An example of the application of the two filters is provided in Fig. 4.

Subsequently, in the “Frequency Analysis” block, first a vector of frequencies on which to estimate the Power Spectral Density of the signal is defined. The boundary frequencies  $f_{min}$ ,  $f_{max}$  are determined by considering:

- The initial guess of the signal period (only the frequencies in the neighbourhood of the frequency associated to the guess are considered).

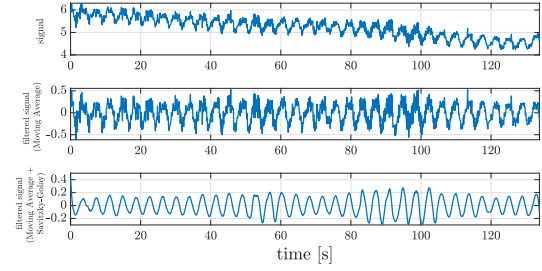


Figure 4. Acquired signal before and after filtering using a Moving Average filter and a Savitzky-Golay filter

- The maximum frequency derived from the Nyquist theorem.
- The maximum expected period for a tumbling RSO, set at 100 seconds.
- The duration of the observation window.

Given the interval of frequencies, the Lomb-Scargle Periodogram is applied to estimate the signal PSD. From this, three candidate periods of the signal are identified, corresponding to the inverse of the frequencies of the highest peaks in the PSD. These three periods are then post-processed in the “Post-Processing” block to determine the most likely period associated with the tumbling motion  $P_1$ . The techniques employed include:

- Close Peaks Merging: weighted merging of peaks in the PSD that occur at very close frequencies. In particular, if the frequency difference is less than 5% of the maximum frequency and the power of one peak is at least 1/5 of the power of the other, the two peaks are merged.
- Identification of multiples of the estimated period using the initial estimate: the periods associated with the remaining peaks are checked to see if they are similar to the period initial estimate or if they are multiples or sub-multiples of it. A 5% margin is used to define these multiplicities (for instance, a value is considered a sub-multiple of another if the relative difference between twice that value and the other is less than 5%). The period (or its multiple/sub-multiple) closest to the period first guess is then returned to the user.

An example of the application of these two procedures is provided in Fig. 5.

### Mode #1.2 : First Guess for $P_1$ Unavailable

Fig. 6 addresses the scenario where no initial estimate of the RSO tumbling period is available. To activate this pipeline, which starts at user's request, all that is required is to deactivate the *firstGuessflag*. As a

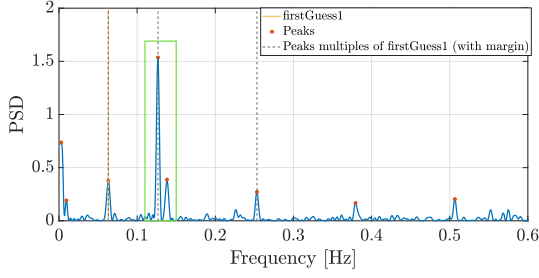


Figure 5. Signal PSD (blue) with key frequency markers. The orange line indicates the frequency associated with the first guess for  $P_1$ , while red dots highlight estimated peaks. The black dashed lines mark estimated peaks that are multiples of the first guess frequency (considering the defined margins). The green box encloses two closely spaced peaks, where the Close Peaks Merging technique is applied.

consequence, and unlike Mode #1.1, no first guess of the tumbling period needs to be provided as input.

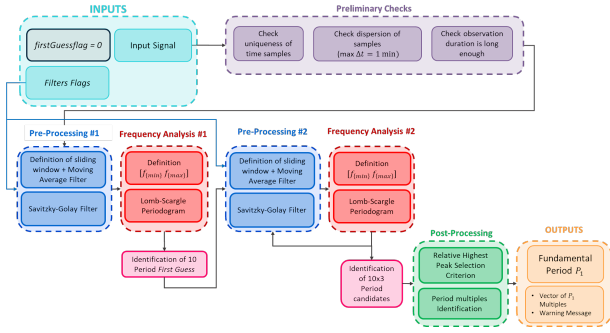


Figure 6. Flow Diagram (Mode #1.2)

The “Preliminary Checks” block performs the same validations seen for Mode #1.1. However, in this case, to verify that the signal duration is sufficient, the lower limit for the signal duration is here set differently. Specifically, it is defined as twice the 75th percentile of a distribution of tumbling periods of 11190 objects, which is found to be 23.87 s. This distribution was obtained from the MMT-9 database [23], accessed in May 2024, as shown in Fig. 7.

If these checks are successful, the signal is pre-processed in the “Pre-Processing #1” block. Even in this case, the user can control the pre-processing by enabling or disabling the moving average filter flag and the Savitzky-Golay filter flag. For the moving average filter, the sliding window size is set to 2 seconds. Subsequently, in the “Frequency Analysis #1” block, the vector of frequencies on which to estimate the PSD is defined by computing  $f_{min}$ ,  $f_{max}$  and taking into account the same constraints seen in Mode #1.1, except for the first one that is related to the availability of the first guess. Given the interval of frequencies, the Lomb-Scargle Peri-

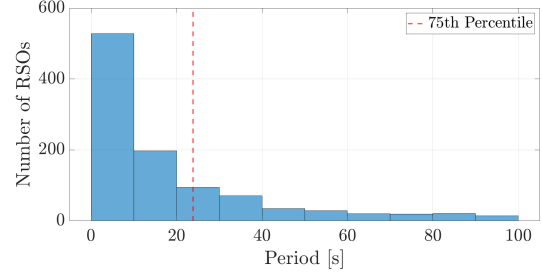


Figure 7. MMT-9 database [23] Periods distribution (accessed in May 2024)

odogram is applied to compute the signal PSD. From this, ten candidate periods of the signal are identified, corresponding to the inverse of the frequencies of the highest peaks in the PSD. These ten periods are then treated as initial estimates of the RSO tumbling period. Each first guess is iteratively fed into the “Pre-Processing #2” and “Frequency Analysis #2” blocks along with the signal in time, in a way similar to Mode #1.1. Thus, for each initial guess, three candidate periods are estimated, resulting in a matrix of 10x3 candidate periods at the end of the iteration.

In the “Post-Processing” block, the Relative Highest Peaks Selection Criterion is applied. According to this method, for each row of the 10x3 matrix, the ratio of the highest peak (i.e. the one associated with the first period of the row) to the average of the peaks associated with all the periods of this row is computed. The candidate with the maximum ratio is chosen and returned as the tumbling period  $P_1$  of the object. Then, if the other elements of the chosen row are multiples or sub-multiples of the returned period, they are also included in a separate vector and returned along with a warning message alerting the operator.

### 3.2. Mode #2

When *SecondPeriodflag* is activated, the pipeline adds a time-domain optimization step to the frequency-domain analysis described above (regardless of whether it is executed in Mode #1.1 or #1.2). A technique inherited from asteroid tumbling estimation literature is applied in a way similar to [2]. After identifying potential initial conditions, the two-dimensional Fourier series that best fits the input data is found through an optimization procedure. This allows to identify the second dominant period  $P_2$ , with the aim of obtaining a comprehensive assessment of the RSO rotation and precession motions. Even in this case, two sub-pipelines can be distinguished, according to the case where an initial guess of  $P_2$  is available or not.

#### Mode #2.1: First Guess for $P_2$ Available

Fig. 8 illustrates the scenario in which an initial guess for the second fundamental period is provided. The process

involves a double-optimization approach.

The algorithm begins by defining the initial guess (the user-supplied input), as well as the lower and upper boundary values for the period  $P_2$  to be found. These boundaries are derived from the frequency limits, determined using the same approach as in the “Frequency Analysis” block for Mode #1.1.

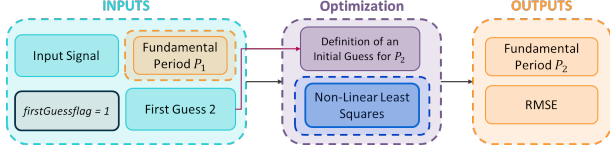


Figure 8. Flow Diagram (Mode #2.1)

Next, a non-linear least squares optimization is performed, as detailed in Fig. 9.

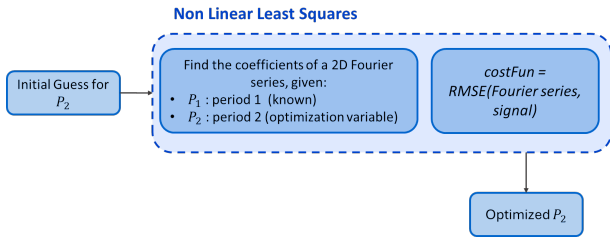


Figure 9. Flow Diagram of the optimization procedure (Mode #2.1)

Given the input signal, the previously computed first period  $P_1$ , and the optimization variable  $P_2$ , the algorithm computes, through an inner optimization procedure, the Fourier coefficients of a two-dimensional Fourier series  $F(t)$  that best fits the input data, the formulation of which is provided in Equation 1. The order  $m$  chosen for the Fourier series is 4, which appears sufficient to capture the trend of the input signal without excessively increasing the number of coefficients.

$$\begin{aligned}
 F(t) = & C_0 + \sum_{i=1}^m \left( C_{i0} \cos\left(i \frac{2\pi}{P_1} t\right) + S_{i0} \sin\left(i \frac{2\pi}{P_1} t\right) \right) \\
 & + \sum_{j=1}^m \sum_{i=-m}^m \left( C_{ij} \cos\left(\left(i \frac{2\pi}{P_1} + j \frac{2\pi}{P_2}\right) t\right) \right. \\
 & \left. + S_{ij} \sin\left(\left(i \frac{2\pi}{P_1} + j \frac{2\pi}{P_2}\right) t\right) \right).
 \end{aligned} \tag{1}$$

In this concurrent optimization procedure, both the second fundamental period  $P_2$  and the Fourier coefficients are refined to minimize the cost function, that is defined as the RMSE between this Fourier model and the input signal. Finally, the module returns the optimized  $P_2$  and the RMSE of the two-dimensional fit, allowing the user to assess the quality of the final solution.

## Mode #2.2: First Guess for $P_2$ Unavailable

Fig. 10 illustrates the scenario where no initial guess for  $P_2$  is provided. The process in Mode #2.2 is similar to that in Mode #2.1, with the key difference being the method used to define the initial guess for the optimization procedure.

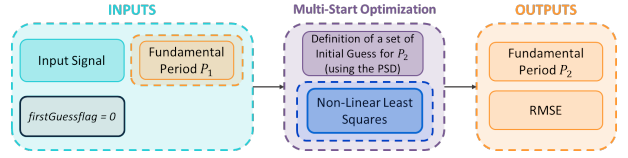


Figure 10. Flow Diagram (Mode #2.2)

In this mode, the signal PSD is retrieved and the first ten peaks are identified. From these, the peak corresponding to the first estimated period  $P_1$  and its multiples or sub-multiples are removed. Additionally, spurious peaks are eliminated; that is, if two peaks are very close together and one has a significantly lower associated power than the other, only the one with the highest power is retained. The remaining peaks are then used as initial guesses for the optimization procedure, as in the example shown in Fig. 11.

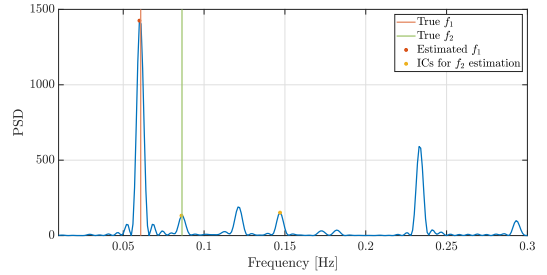


Figure 11. Signal PSD (blue) with key frequency markers. The orange and green lines represent the frequencies associated to the true period  $P_1$  and  $P_2$  respectively, the red dot marks the frequency associated to the estimated  $P_1$  and the yellow dots the identified candidate frequencies for the optimization procedure.

The lower and upper boundary values for the periods, instead, are determined from the boundary frequencies, following the same approach as in the “Frequency Analysis #1” block for Mode #1.2.

A non-linear least squares optimization is subsequently performed for each possible initial guess, as shown in Fig. 12. Similar to Mode #2.1, this process optimizes both the second fundamental period  $P_2$  and the Fourier coefficients to minimize the RMSE between a two-dimensional, fourth-order Fourier series and the input data.

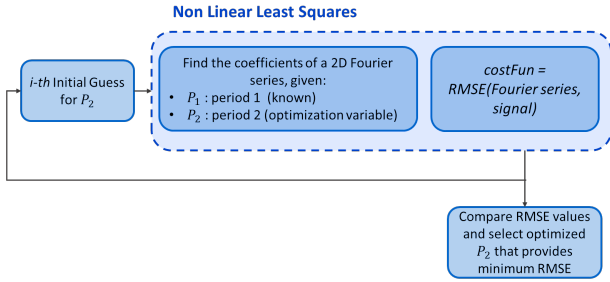


Figure 12. Flow Diagram of the optimization procedure (Mode #2.2)

Table 1. Orbital Parameters

$a$ [km]	$e$ [-]	$i$ [deg]	$\Omega$ [deg]	$\omega$ [deg]
7345	7.52e-04	66.00	81.47	320.50

## 4. NUMERICAL RESULTS

The performance of the module has been tested on simulated RCS measurements, as presented in Section 4.1. Then, to assess its effectiveness in real-case scenarios, the tool was tested on light curves from the MMT-9 database [23], as detailed in Section 4.2.

### 4.1. Test on Simulated RCS Data

The acquisition of RCS data has been simulated for a satellite modeled as a parallelepiped with dimensions  $3 \times 1 \times 5$  m and a uniformly distributed mass, with faces exhibiting varying reflectivity properties. The satellite is assumed to be in an arbitrary LEO with the parameters specified in Tab. 1. No external torques are applied to the object, ensuring that its tumbling dynamics and kinematics remain unaffected by external forces.

The radar station is modeled as a monostatic, stationary system located at the origin of an inertial reference frame and operating in tracking mode to follow the object.

For all simulated scenarios, the initial attitude is kept constant, with Euler angles (describing the orientation of the target body reference frame with respect to the inertial frame) arbitrarily set to  $[1.98, 12.28, -1.98]$  degrees. However, different initial conditions for the angular velocity and varying observation window durations have been considered.

By propagating the initial attitude vector (defined by the initial Euler angles and angular velocity vector) over the observation window, the ground-truth values for the precession period  $P_1$  and rotation period  $P_2$  were determined for each case.

The simulated examples are presented in Tab. 2. For each case, the table includes the following information:

- Example ID;
- Satellite initial angular velocity vector  $\omega_0$ ;
- Duration of the observation window  $d$ ;
- Ground truth values for the precession and rotation periods  $P_1$  and  $P_2$ ;
- Selected operating mode of the RSO Characterization Module; if a first guess of one of the periods is provided, which one is specified. This initial guess is generated by adding noise to the ground-truth value;
- Values estimated for  $P_1$  and  $P_2$  by the RSO Characterization Module;
- Relative error between the ground-truth and the estimated values.

Examples E1.1 and E1.2 simulate a scenario where the RCS time-series is characterized by a single period. The simulation conditions remain the same across all three examples, with the only difference being the operating mode used to analyze the acquired signal. Specifically, in Example E1.1, the *secondPeriodflag* is deactivated, and a first guess for  $P_1$  is provided. Under these conditions, the estimated tumbling period closely matches the ground-truth value, with a relative error of 0.18%. In Example E1.2, instead, no first guess is available, and the estimated value corresponds to half of the actual period rather than the full period. This discrepancy likely arises from the geometric symmetry of the object, which can cause the algorithm to identify a submultiple of the true period. However, by simply doubling the estimated value, the correct period is recovered, reducing the relative error to just 0.14%.

Examples E2.1, E2.2, E2.3, on the other hand, refer to cases where the simulated signal is characterized by two periodicities, requiring the *secondPeriodflag* to be activated. In E2.1, an initial guess is provided for  $P_2$ , whereas in E2.2, an initial guess is assumed for  $P_1$ . No initial values are instead provided for Example E2.3. In all cases, the relative error remains below 0.5% for both  $P_1$  and  $P_2$ .

The same applies to Examples E3.1, E3.2, E3.3. However, for Example E3.1 and E3.3, the estimated  $P_1$  (and also  $P_2$  in E3.3) appears to be incorrect. By analyzing the frequencies associated with these estimated values, it becomes evident that they are a linear combination of those corresponding to the true periods. Specifically, being  $f_1$  and  $f_2$  the frequencies associated to the ground-truth  $P_1$  and  $P_2$ , respectively, in Example E3.3 the first estimated value corresponds to  $f_1 + 2f_2$ , while the second to  $f_1 + f_2$ . This issue is a known limitation in this type of analysis and has been documented in previous studies [2] [20].

Overall, looking at the last column, it is possible to observe that the relative error remains relatively small (lower than 2%) for both  $P_1$  and  $P_2$ , except for Examples E1.2, E3.1, and E3.3, due to the reasons previously discussed. For illustrative purposes, Fig. 13 presents the output of Example E3.2.

Table 2. Results of the RCS Characterization Module on simulated RCS data

Ex. ID	$\omega_0$ [rad/s]	$d$ [min]	Operating Mode	Ground-Truth [s]		Estimates [s]		Rel. Error [%]	
				$P_1$	$P_2$	$P_1$	$P_2$	$P_1$	$P_2$
E1.1	[0.3 0.8 0]	3	#1.1 ( <i>FirstGuess1</i> )	7.46	nan	7.47	-	0.18	-
E1.2	[0.3 0.8 0]	3	#1.2	7.46	nan	3.73	-	49.93	-
E2.1	[0 0.8 1.3]	2	#2.1 ( <i>FirstGuess2</i> )	6.01	9.35	5.99	9.37	0.33	0.21
E2.2	[0 0.8 1.3]	2	#2.2 ( <i>FirstGuess1</i> )	6.01	9.35	6.02	9.34	0.17	0.11
E2.3	[0 0.8 1.3]	2	#2.2	6.01	9.35	5.99	9.37	0.33	0.21
E3.1	[0.04 0.03 0.25]	6	#2.1 ( <i>FirstGuess2</i> )	63.17	38.11	14.76	38.27	76.63	0.42
E3.2	[0.04 0.03 0.25]	6	#2.2 ( <i>FirstGuess1</i> )	63.17	38.11	62.50	38.64	1.06	1.39
E3.3	[0.04 0.03 0.25]	6	#2.2	63.17	38.11	14.76	24.02	76.63	36.97

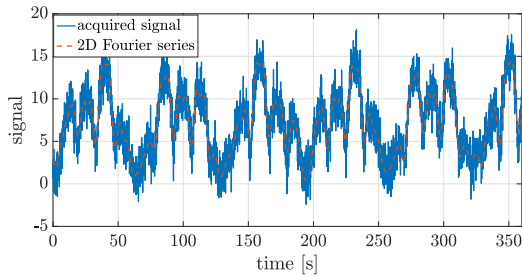


Figure 13. Example E3.2: Simulated acquired RCS time series (blue line) and 2D Fourier series (dashed red line) with periodicities equal to the estimated periods

Regarding computational time, when *SecondPeriodFlag* is deactivated, the module can determine the dominant period of the signal within 5 seconds. In contrast, when it is activated, the module returns the outputs within a maximum of 8 minutes.

#### 4.2. Validation on Real Data

Since no public database of RCS measurements is available, it was not possible to validate the pipeline using real RCS data. Instead, optical light curves were used for validation, specifically those available in the publicly accessible database of the MMT-9 optical sensor referenced in [23]. This database provides a rotation period for each light curve associated with a periodic object. However, since only a single period is reported for each light curve, only the fundamental period  $P_1$  was estimated, assuming no prior knowledge on this value (i.e., running the module in Mode #1.2).

Fig. 14 presents the results of this procedure applied to 30 observations of the H-2A rocket body (norad 26899) downloaded from the database. The yellow dots represent the period values recorded in the database for each observation (with the corresponding date shown on the x-axis), while the green dots indicate the estimated values. The continuous red lines represent a confidence inter-

val. To define it, a first-order polynomial (linear trend)  $poly_1$  was fitted to the yellow dots. The RMSE was then computed between  $poly_1$  and the yellow dots. Hence, the confidence interval was obtained by adding and subtracting three times the RMSE from the polynomial fit ( $poly_1 \pm 3 RMSE$ ).

Any green points that fall within this interval are considered good estimates, totaling 14 out of 30 (46.67%). However, 14 other points (46.67%), although not within the confidence area, lie within the dashed red lines, which represent submultiples of the confidence interval (obtained by dividing it by 2 and by 4). This suggests that these estimated values are submultiples of the true values. Such a pattern aligns with previously observed shortcomings (Examples E1.2, E3.1, and E3.3) and is likely due to geometric symmetries in the target, which, in this case, is a rocket body with a cylindrical shape [19]. The remaining 2 points, accounting for 6.67% of the total, are instead close to but outside the confidence intervals.

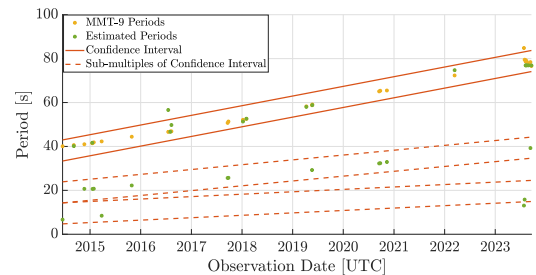


Figure 14. Results of the RSO Characterization Module (Mode #1.2) on 30 optical observations of the H-2A rocket body (norad 26899)

## 5. CONCLUSIONS

In this section, the key operational limits of the module (Section 5.1) and the foreseen future steps (Section 5.2) are outlined.

## 5.1. Operational Limits

The accuracy of the results provided by the module heavily relies on the quality of the measurements. Factors such as low signal-to-noise ratio, insufficient sampling rate, large gaps in the measurement data, and short observation windows can all lead to inaccurate period estimates. Moreover, the characteristics of the target object, including its shape and material properties, can significantly affect its measured radar cross section and light curve, potentially complicating the interpretation of the measurements and thus the period estimation. For instance, the observation of objects with evident geometrical symmetry may produce signals that erroneously lead to the estimation of the semi-period of the tumbling target, especially in the absence of prior information, as seen in Example E1.2 and in Section 4.2. Moreover, rotating instruments on-board may cause misinterpretations of the estimated periods.

Finally, as observed in Examples E3.1 and E3.3, it is generally difficult to confidently state that the first period corresponds to the precession period and the second to the rotation period with no initial guess on any of them. While this occurs in most simulated cases, there are instances where the result may be a linear combination of the two values.

## 5.2. Future Steps

Some improvements are planned to enhance the pipeline. First, the Lomb-Scargle Periodogram will be combined with other algorithms (e.g., Phase Dispersion Minimization) to improve result accuracy. Moreover, additional metrics will be explored to eliminate spurious peaks and identify the most relevant ones in the signal PSD [21] [4]. Another essential step is to validate these methodologies with real observational data, particularly for radar measurements, which have so far only been tested in a simulated scenario. This will help refine the pipeline, ensuring that its performance meets practical requirements and operational constraints.

A significant addition to the pipeline will be the integration of a classification block. This would allow for the distinction between stable and rotating objects, ensuring that the periods estimation pipeline is applied only to the latter. To achieve this, machine learning techniques will be explored, inspired by methodologies such as those outlined in [17] and [18]. Indeed, machine learning methods are particularly effective for classification tasks; however, their application in this field faces the challenge of limited datasets for proper training.

Finally, data-fusion techniques will be explored to integrate multiple observations from the same or different sensors, enhancing the ability to accurately characterize the tumbling motion of the observed RSO.

## ACKNOWLEDGMENTS

This research presented received funding as part of the work developed for the project “Servizi inerenti alla realizzazione di un’infrastruttura HW e SW presso il CGS/Matera” from the Italian Space Agency ASI-IHS infrastructure for space surveillance and tracking, under the Next Generation UE/PNRR framework, contract number 2023-14-I.0.

## REFERENCES

1. T. Schildknecht, J. Šilha, “Determining and Modeling Space Debris Attitude States by Fusing Data from different Observation Techniques”, *7th European Conference on Space Debris* (2017)
2. C. Benson, D.J. Scheeres, N. Moskovitz, “Light Curves of Retired Geosynchronous satellites”, *7th European Conference on Space Debris* (2017)
3. T. Yanagisawa, H. Kurosaki, “Shape and motion estimate of LEO debris using light curves”, *Advances in Space Research - Volume 50 - Issue 1* (2012)
4. G. Isoletta, R. Opromolla, G. Fasano, “Attitude Motion Classification of Resident Space Objects Using Light Curve Spectral Analysis”, *Advances in Space Research* (2024)
5. N.R. Lomb, “Least-Squares Frequency Analysis of Unequally Spaced Data”, *Astrophysics and Space Science - Volume 39 - P. 447–462* (1976)
6. J.D. Scargle, “Studies in Astronomical Time Series Analysis. II. Statistical Aspects of Spectral Analysis of Unevenly Spaced Data”, *Astrophysical Journal - Volume 263 - P. 835–853* (1982)
7. S. Larsson, “Parameter estimation in epoch folding analysis”, *Astronomy & Astrophysics Supplement Series 117* (1996)
8. F. Santoni, E. Cordelli, F. Piergentili, “Determination of disposed-upper-stage attitude motion by ground-based optical observations”, *Journal of Spacecraft and Rockets - Volume 50 - Number 3* (2013)
9. S. Zhao, M. Steindorfer, G. Kirchner, Y. Zheng, F. Koidl, P. Wang, W. Shang, J. Zhang, T. Li, “Attitude analysis of space debris using SLR and light curve data measured with single-photon detector”, *Advances in Space Research - Volume 65 - Issue 5* (2020)
10. A. Burton, C. Frueh, “Two Methods For Light Curve Inversion For Space Object Attitude Determination”, *8th European Conference on Space Debris* (2021)
11. G. P. Badura, C. R. Valenta, “Physics-Guided Machine Learning for Satellite Spin Property Estimation from Light Curves”, *Advanced Maui Optical and Space Surveillance Technologies Conference* (2023)
12. D. A. Bosma, F. Uysal, “First Results of Attitude Estimation using RCS Time Series for Space Domain Awareness”, *IEEE Radar Conference* (2024)

13. J. Lyu, W. Zhong, H. Liu, Y. Geng, D. Ben, "Novel Approach to Determine Spinning Satellites' Attitude by RCS Measurements", *Journal of Aerospace Engineering – Volume 34 – Number 4* (2021)
14. M.A. Stevenson, M. Niccols, C. Rosner, "Space Object Attitude Stability Determined from Radar Cross-Section Statistics", *Advanced Maui Optical and Space Surveillance Technologies Conference* (2019)
15. D. McKnight, S. Fiore, T. Schildknecht, J. McKune, D. Engelhardt, "Rocket Body Tumbling Assessment Through Radar, Optical Telescope, and Imaging", *75th International Astronautical Congress* (2024)
16. A. Savitzky, M.J.E Golay, "Smoothing and Differentiation of Data by Simplified Least Squares Procedures", *Analytical Chemistry*, 36(8):1627-1639 (1964)
17. R. Furfaro, R. Linares, V. Reddy, "Space Objects Classification via Light-Curve Measurements: Deep Convolutional Neural Networks and Model-based Transfer Learning", *Advanced Maui Optical and Space Surveillance Technologies Conference* (2018)
18. Á. Gallego, C. Paulete, M. Torras, A. de Andrés, A. M. Antón, "RSO Characterization and Attitude Estimation with Data Fusion and Advanced Data Simulation", *Advanced Maui Optical and Space Surveillance Technologies Conference* (2023)
19. T. Hrobár, J. Šilha, M. Zigo, P. Jevčák, P. Patole, T. Schildknecht, "Attitude determination of cylindrical rocket bodies by using simultaneous bistatic photometric measurements", *Advanced Maui Optical and Space Surveillance Technologies Conference* (2023)
20. M. Kaasalainen, "Interpretation of lightcurves of precessing asteroids", *Journal A&A – Volume 376 – Number 1* (2001)
21. A. L. H. Lam, J. Margot, E. Whittaker, N. Myhrvold, "Determination of 1929 Asteroid Rotation Periods from WISE Data", *The Planetary Science Journal - Volume 4 - Number 4* (2023)
22. M.F. Montaruli, G. Purpura, R. Cipollone, et al. "An orbit determination software suite for Space Surveillance and Tracking applications", *CEAS Space Journal - Volume 16 - Issue 5* (2024)
23. *Satellites identified in MMT data*. Available online: <http://mmt9.ru/satellites/> (accessed in May 2024)